PHYSICAL REVIEW B **68**, 064204 (2003)

Density-functional calculations of the liquid deuterium Hugoniot, reshock, and reverberation timing

Michael P. Desjarlais*
Pulsed Power Sciences Center, Sandia National Laboratories, Albuquerque, New Mexico 87185, USA

(Received 18 April 2003; published 21 August 2003)

The principal Hugoniot of liquid deuterium is calculated with density-functional methods. Particular attention is paid to the convergence of thermodynamic quantities with respect to the plane-wave cutoff energy and other simulation constraints. In contrast to earlier density-functional calculations, it is found that the principal Hugoniot results are in very good agreement with gas-gun data at lower pressures and compression ratios. The results at higher pressures are in very good agreement with data from magnetically launched flyer plates and show slightly less compression than earlier density-functional calculations. In addition to the principal Hugoniot, reshock states from a sapphire anvil and third-shock reverberation timings are also calculated. The latter are found to be in very good agreement with recently published results from magnetically launched flyer-plate experiments.

DOI: 10.1103/PhysRevB.68.064204 PACS number(s): 64.30.+t, 62.50.+p, 05.30.−d, 02.70.Ns

I. INTRODUCTION

Recent years have seen an explosion of interest in the equation of state (EOS) of dense hydrogen and its isotopes. Much of the excitement has been stimulated by data from laser-driven shock experiments[1,2] at Livermore National Laboratory, which indicate a peak single-shock compression for deuterium of about 6, and subsequent magnetically launched flyer-driven shock experiments[3,4] at Sandia National Laboratories, which indicate a peak compression closer to 4.3. At lower pressures, both the laser experiments and the flyer experiments produce results that are consistent with earlier gas-gun driven shock experiments,[5] which are considered to be highly accurate, utilizing a well proven technique for achieving high compression states. This experimental discrepancy at higher pressures has driven numerous theoretical and experimental attempts to further our understanding of dense hydrogen and hopefully find a resolution to the differences. An improved understanding of the hydrogen EOS has immediate and broad application to models for the interiors of the giant planets, astrophysical plasmas, warm dense matter, and inertial confinement fusion.

Quantum molecular-dynamics (QMD) simulations are a powerful tool for exploring the equation of state of warm dense matter, where the thermal occupation of excited electronic states is, in general, non-negligible and the ions are strongly coupled. This work explores the properties of shocked deuterium within the framework of the finite temperature density functional theory (FT-DFT) of Mermin.[6] There have been several earlier treatments of the hydrogen EOS and Hugoniot within the DFT/QMD approach.[7–9] However, the relevance of previous density-functional calculations to the deuterium EOS has sometimes been questioned because earlier calculations were unable to reproduce data from gas-gun experiments,[5] which are consistent with both laser and flyer experiments.

To address this question, and to further illuminate the use of density-functional methods for equation of state studies in the warm dense matter regime, several simulation constraints affecting the convergence of calculations of this sort are examined with emphasis on the convergence of thermodynamic quantities. In addition to the principal Hugoniot, reflected shock states with a sapphire anvil and third-shock reverberation timings are also calculated, generating a multitude of highly converged DFT results to be compared with experiments over a broad range of densities and temperatures. We expect that these results will also serve as a useful benchmark for future DFT/QMD work that employs density functionals that go beyond the local-density approximation(LDA).

II. COMPUTATIONAL METHOD

For calculations of the principal Hugoniot, we are primarily concerned with the total pressure and energy of the deuterium for various density and temperature states. To obtain these thermodynamic quantities, quantum molecular-dynamics simulations are performed using VASP (Vienna *ab initio* simulation program), a plane-wave density-functional code developed at the Technical University of Vienna.[10–13] The DFT exchange and correlation functionals are calculated at the level of the generalized gradient approximation (GGA) using the parametrization of Perdew-Wang 91.[14] The density is fixed by the total volume of the cubic supercell and the ion temperature is regulated with a Nosé-Hoover thermostat.[15–17] The electronic temperature is fixed by Fermi weighting the occupation of the bands. The forces on the ions and the electronic contribution to the pressure are computed quantum mechanically at each QMD time step following the Hellmann-Feynman theorem,[18] however the ion motion is advanced classically and zero-point vibrations, for example, are not included. The electronic wave function is relaxed at each time step under the Born-Oppenheimer approximation, which assumes decoupled electronic and ionic time scales. Pressures and energies are obtained from molecular-dynamics runs covering sufficiently long times to ensure adequate convergence as indicated by cumulative averages taken with different starting times. The thermodynamic quantities are taken as averages over an equilibrated portion

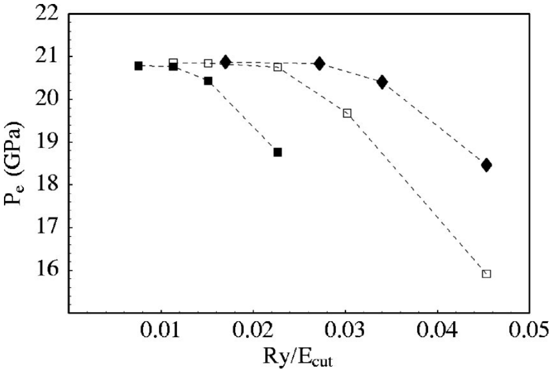

FIG. 1. The convergence of the electronic contribution to the pressure is shown plotted versus Ry/E_{cut} for a hard PAW potential (filled squares), a soft PAW potential (open squares), and a US pseudopotential (diamonds). The pressure values are the averages of ten configurations taken from a highly converged QMD run, rerun with different values of the plane-wave cutoff E_{cut}.

of the cumulative averages. Typical total simulation times are of the order of 1–2 ps, typical velocity-velocity autocorrelation decay times are of the order of tens of femtoseconds, and time steps are of the order of 0.2 fs.

The VASP code uses a plane-wave basis set to represent the electronic wave function. The accuracy of this representation is determined in large part by the chosen maximum energy, or cutoff energy E_{cut}, of the plane waves used in this expansion. The electronic contribution to the pressure is much slower to converge with the plane-wave cutoff energy than the total energy and care must be taken to ensure that the cutoff is sufficiently high to obtain accurate forces and pressures. The electronic pressure convergence with inverse cutoff energy is illustrated for a hard projector-augmented-wave (PAW) potential (filled squares[19]), a soft PAW potential (open squares[19]), and an ultrasoft pseudopotential (USPP) (diamonds[20]) in Fig. 1. The pressure values shown are the averages of ten configurations taken from a highly converged QMD run on the principal Hugoniot which were then rerun with different values of the plane-wave cutoff E_{cut}. This approach was used to separate the cutoff effect on the pressure from the dynamics and inherent fluctuations, resulting in a much cleaner comparison. The results of distinct QMD runs for the different cutoff energies hint at a slightly stronger dependence on the cutoff energy, suggesting a cumulative effect that eventually results in differing trajectories.

The convergence behavior of the various potentials can be compared on equal footing by plotting the pressure versus the kinetic-energy error for a given cutoff energy, as shown in Fig. 2. The kinetic-energy error is a well-defined quantity for a given atomic pseudopotential and is the kinetic energy in the atomic wave function above the cutoff.[21] The kinetic-energy error is a strong function of E_{cut}, scaling as E_{cut}^{-4}. The error in the pressure is linear in the kinetic-energy error for small values of this error. The slope of this linear dependence does depend, in general, on the atomic configuration. Based on the results of Fig. 1 and our need to simulate high densities in the second and third shocks, we use the hard core PAW potential and a cutoff energy of 1200 eV. The error in the electronic contribution to the energy $\delta E_e/E_e$ is much smaller over the range of Fig. 2 and is of the order of $(\delta P_e/P_e)^2$. Plane-wave cutoff energies that give high convergence of the energy may be insufficient for pressure convergence.

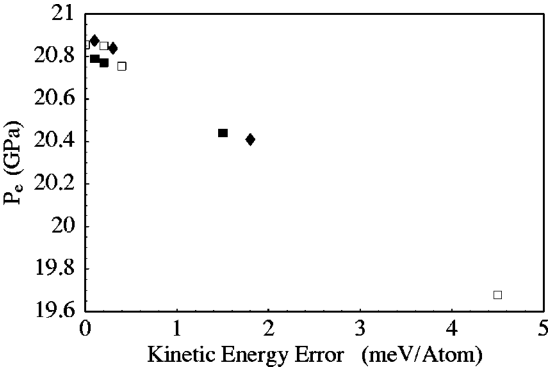

FIG. 2. The convergence of the electronic contribution to the pressure is shown plotted versus the kinetic-energy error.

In order to obtain accurate forces in the QMD runs, we also evaluate the projection operators associated with the nonlocal part of the ionic potential (USPP or PAW) in reciprocal space. This removes a known source of error in the forces in exchange for less efficient computations. In addition, we were not able to demonstrate a systematic convergence of the pressure with cutoff energy when evaluating the projection operators in real space.

The **k**-point set used to represent the Brillouin zone was also explored. For these very disordered systems the choice of **k** points is not nearly as critical as in a highly ordered solid. We found a very slight increase in pressure (about 0.2–0.3 GPa) when using Baldereschi's mean value point[22] instead of the Γ point, $\mathbf{k}=(0,0,0)$. Higher-order **k**-point sets[23] gave no further increase. For principal Hugoniot pressures below 60 GPa, we use the mean value point. For all other calculations we use the Γ point.

For the calculations presented here we made use of 128 atoms in the supercell. Several simulations were also run with up to 256 atoms in the supercell to test size effects for different densities and pressures, but the results for the most part were not significantly different. One exception, to be discussed further in Sec. III, is in the molecular dissociation regime.

As was first explored for the dense hydrogen Hugoniot in Ref. 9, we also examined the effect of spin through the local spin-density approximation (LSDA) and in agreement with that earlier work found no significant difference between GGA-LDA and GGA-LSDA results. Histograms of the first and second nearest-neighbor populations show that for the densities considered here the atoms generally remain within the distance over which the LDA and LSDA energies are the same, so the lack of difference between the two approaches is not surprising. To take advantage of a substantial computational savings, we performed our calculations without spin (GGA-LDA).

III. PRINCIPAL HUGONIOT

The principal Hugoniot is the locus of single-shock end states (E_1,P_1,V_1) satisfying inherently the energy condition[24]

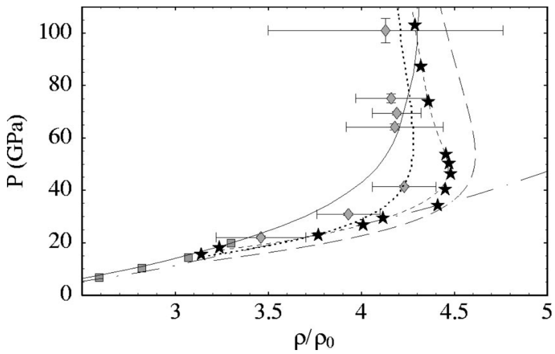

FIG. 3. Liquid deuterium principal Hugoniot results (stars) along with gas-gun data [squares (Refs. 5)] and uncertainty-weighted-average flyer-plate data [diamonds Refs. 3 and 4]. Also shown for comparison are Kerley98 [solid line (Ref. 26)], LBKC-GGA Hugoniot [long-dashed line (Ref. 7)], the linear-mixing model [dot-dashed line (Ref. 28)], and the tight-binding model [dotted line (Ref. 29)]. The short-dashed line is a fit to our results generated with thermodynamically consistent corrections to the LBKC-GGA EOS.

$$E_1 - E_0 = \frac{P_1 + P_0}{2}(V_0 - V_1), \tag{1}$$

where E is the internal energy, P is the pressure, and V is the volume. The subscripts 0 and 1 refer to the (fixed) initial and (various) first-shock states, respectively. In addition, relations between the particle speed u_p, shock speed U_s, and density compression ρ_1/ρ_0 follow from the conservation of mass and momentum;[24] $\rho_1/\rho_0 = U_s/(U_s - u_p)$ and $U_s u_p = (P_1 - P_0)/\rho_0$.

The reference state of the liquid deuterium is taken to be 0.1703 g/cm^3 at 20 K and zero pressure. The initial energy per atom is determined from a DFT/GGA calculation of the cold liquid deuterium at the reference density. The zero-point energy $\frac{1}{4}h\nu_{vib}$/atom (not included in these DFT/QMD calculations) is then added, resulting in a reference energy in excellent agreement with an essentially exact calculation for an isolated deuterium dimer.[25]

In searching for highly converged solutions to Eq. (1), we have made extensive and profitable use of the DFT/GGA EOS of Lenosky, Bickham, Kress, and Collins,[7] hereafter referred to as LBKC-GGA. Following an initial calculation in the vicinity of the Hugoniot, local corrections to the LBKC-GGA EOS, $\delta E(\rho,T)$ and $\delta P(\rho,T)$, were obtained and used to iterate the density and temperature to a new prediction for a density and temperature along the principal Hugoniot. This procedure converged very rapidly. In general, these corrections were most significant in pressure with an increase in the range of 1–3 GPa.

The results of the principal Hugoniot calculations are shown (stars) in Fig. 3 along with gas-gun data (squares[5]) and uncertainty-weighted-average flyer-plate data (diamonds[3,4]). Shown for comparison are two chemical models: Kerley's 1998 revision (Kerley98, solid line[26]) of his earlier SESAME model[27] and Ross' linear-mixing model (dot-dashed line[28]). These two models represent, more or less, the extremes of the many chemical models in terms of compression at a given pressure. The LBKC-GGA Hugoniot is shown with a long-dashed line[7] and the tight-binding model with a dotted line.[29] Not shown in Fig. 3, but important nevertheless, are the laser-driven shock data,[1,2] which largely follow the linear-mixing model and reach compression ratios of 6 near 100 GPa, and *ab initio* results from path-integral Monte Carlo (PIMC) calculations[30] above 50 GPa, which on this figure would follow closely the Kerley98 curve.

Note that the two lowest pressure points from our calculations (at compressions of 3.139 and 3.236) are in very good agreement with the upper range of the gas-gun data.[5] For these two states, because of the low temperature and well-defined dimer population, the zero-point energy contributes a small amount (<0.02 eV/atom) to the expected energy[31] and is added to the total energy E_1 of these states as well. Not doing so would lead to slightly higher Hugoniot pressures at the same compression. Our temperatures for these points are 3300 K and 3800 K respectively. Interpolating between the data in Fig. 8 of Ref. 32 to obtain experimental first-shock temperatures for the same compressions, we find 3430 K and 3860 K, respectively. The experimental uncertainty reported is 100–200 K, so the first-shock temperatures found here are also in very good agreement with gas-gun data. This is in contrast to earlier DFT/GGA calculations that found a softer (and cooler) Hugoniot[7] at these compressions. The temperature at various points along the Hugoniot will be discussed further in Sec. V along with results from the second and third shocks.

At higher compressions the results are stiffer throughout than the LBKC-GGA calculations and are generally within (3–5)% (in compression) of the Sandia flyer data and at the high-density end of the weighted-average error bars for the Sandia data. A systematic error of this size in the flyer data is plausible because the impedance-matching technique used in the flyer experiments[3] relies on a computed aluminum release isentrope to infer u_p and the percentage error in U_s or u_p is multiplied by $(\rho_1/\rho_0 - 1)$ when converting to density compression. The (3–5)% difference in compression is equivalent to about a 1% systematic error in either U_s or u_p.

The best agreement overall between the combined gas-gun data and flyer data is still obtained with the semiempirical tight-binding model.[29] However, these new *ab initio* results improve on the tight-binding model in the range of the gas-gun data and show only about 2% more compression at the higher pressures. Our results generally agree quite well with the linear-mixing model for compressions up to 4.4 and pressures up to 35 GPa. Beyond that point, which is in the midst of the dissociation phase in our calculations, our Hugoniot stiffens abruptly, consistent with the Sandia flyer data and in disagreement with linear-mixing and the laser-driven shock data.

Recent DFT/QMD shock simulations[33] have been able to produce a softer Hugoniot response consistent with the laser-driven data and linear-mixing model by employing the artificial electronic mass of the Car-Parrinello method[34] as a free parameter for modeling departures from the Born-Oppenheimer surface. While this work is intriguing, there remains, as of this writing, no direct physical connection

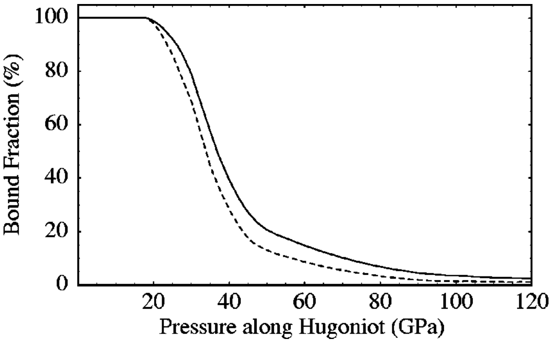

FIG. 4. The percentage of deuterium atoms that remain nearest neighbors (solid line) or mutual nearest neighbors (dashed line) for a time greater than two vibron periods, plotted versus pressure along the Hugoniot.

established between departures from the Born-Oppenheimer surface engendered by the fictitious electronic mass and real departures associated with excited states and close electronic and ionic time scales.

Since the LBKC-GGA EOS is thermodynamically consistent by construction, we generated thermodynamically consistent corrections to the LBKC-GGA EOS that are consistent with our results and valid in the neighborhood of the principal Hugoniot above ≈ 20 GPa. The result is shown in Fig. 3 as the short-dashed line and is generated with $P = P_{\mathrm{LBKC}} + \delta P$ and $(E-E_0) = (E-E_0)_{\mathrm{LBKC}} + \delta(E-E_0)$, where $\delta P = 1.8$ GPa and (in Ry/atom)

$$\delta(E-E_0) = -\delta P\, V - 0.007\,18 + (0.011\, e^{-[(T-7500)/6000]^2} \times [1 - e^{-(T/4000)^2}] - 0.0019).$$

The pressure correction is well approximated with a constant increase of 1.8 GPa. The first term in $\delta(E-E_0)$ is required for thermodynamic consistency and the second term reflects the zero-point energy correction. This simple (but not definitive) correction is sufficient everywhere in the neighborhood of the principal Hugoniot except the dissociation regime, where thermodynamic behavior indicative of a phase change, $(\partial P/\partial T)_V < 0$, has previously been noted.[9,28] The LBKC-GGA EOS and our correction to it do not include this behavior; however, it was demonstrated in Ref. 9 that the negative pressure gradient diminishes with increasing system size. This regime is the one portion of the primary Hugoniot where we observed significant size effects above 128 atoms. At 256 atoms the Hugoniot is slightly smoother near 35 GPa and closer to the fit, but unfortunately the behavior between 128 atoms and 256 atoms is not monotonic; the Hugoniot softened with increasing size before stiffening again, suggesting an enhanced dependence on longer length scales—not surprising in the vicinity of a phase change, in this instance the transition from a molecular to atomic fluid.

In chemical models of dense hydrogen, the relative populations of molecules and atoms figure significantly in the resulting equation of state and Hugoniot. (See Ref. 35 for a recent example and many additional references.) The estimated fraction of atoms participating in bonds in our simulations is shown in Fig. 4 versus pressure along the Hugoniot. The bound fraction is estimated by first counting, for a given snapshot in time, those nearest neighbors that have remained, or will remain, nearest neighbors for a minimum of two deuterium vibron periods—about 22 fs. We then average the results from many snapshots over the entire simulation. For the solid line, the bound fraction is all nearest neighbors (NN's), not necessarily mutual, thus including more complex clusters than dimers in the bound fraction. The dashed line includes only mutual nearest neighbors (MNN's), which restricts the population to dimers. Even at the higher pressures, where the NN population is several times the MNN population, the instantaneous population is still dominated by mutual nearest neighbors. Frequent collisions with other neighboring dimers and atoms make these mutual nearest neighbors short lived, without having as significant an effect on the total nearest-neighbor count. In general, one might further restrict the population to those nearest neighbors that are within some bond cutoff distance, perhaps two or three times the equilibrium atomic separation in the dimer. However, for the densities considered here, bond cutoff distances beyond two times the dimer length were of minor consequence. A precise count of the bound atoms in our QMD simulations would require a complicated analysis of the electronic wave function and correlated motion between neighboring atoms; the above analysis is far simpler and gives results that capture well the behavior observable in animations.

Because of the added requirement of a finite lifetime, our MNN bound fractions at higher pressures are lower than, but entirely consistent with, the results of earlier tight-binding and density-functional calculations.[36,37] The bound fractions found here as a function of density and temperature along our Hugoniot are in very good agreement with the results of PIMC calculations[38] and Ross' linear-mixing model[28] for the same densities and temperatures. For a comparable density, all give 50% dissociation around 10 000 K. The model of Saumon and Chabrier[39] gives somewhat slower dissociation with temperature at comparable densities (50% around 17 000 K), and the fluid variational theory[35] gives significantly slower dissociation with increasing temperature above 15 000 K, reaching 50% dissociation around 25 000 K.

By either measure, nearest neighbor or mutual nearest neighbor, peak compression along the Hugoniot occurs in the vicinity of a bound fraction of 50%. The most rapid change from bound to unbound takes place between 25 and 50 GPa. These results are in good agreement with recent arguments presented by Nellis.[40]

IV. RESHOCK AND REVERBERATION

In a recent paper,[4] an alternative technique for probing the density compression of shocked deuterium is presented that permits a more discriminating comparison of the data and models. This method makes direct use of the timing of the reverberating shock waves in the shocked (and reshocked) deuterium sample. In the following, we present the results of high convergence DFT/QMD calculations of the shocked states needed for comparison with the reverberation timing

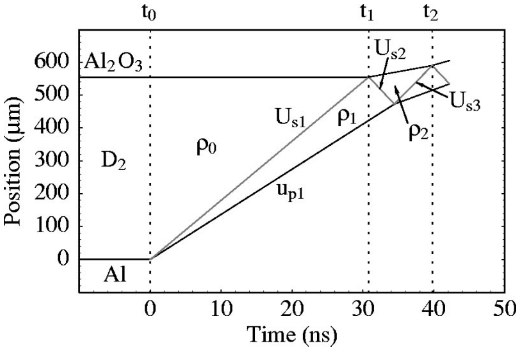

FIG. 5. A time-position diagram of the shock fronts and material interfaces for a reverberation timing experiment.

data. These reverberation calculations require solutions to the additional Hugoniot equations

$$E_2-E_1=\frac{P_2+P_1}{2}(V_1-V_2) \tag{2}$$

and

$$E_3-E_2=\frac{P_3+P_2}{2}(V_2-V_3), \tag{3}$$

where the subscripts 1, 2, and 3 refer to the first, second, and third shock, respectively. The relations between U_s, u_p, and ρ/ρ_0 accompanying Eq. (1) follow analogously in the relative (Lagrangian) frame. A diagram of a reverberation experiment is shown in Fig. 5 (see Ref. 4 for details). A shock wave from the magnetically launched flyer plate travels through the aluminum driver to impact (at t_0) the liquid D_2 which is backed by a sapphire anvil that also serves as a diagnostic window. The first shock reflects off the sapphire anvil at t_1 and creates a reshock state in the D_2. The second shock in turn reflects off the aluminum driver, launching a third shock that arrives back at the D_2-sapphire interface at t_2.

For the second- and third-shock states, a triad of simulations $((\rho_A,T_A),(\rho_B,T_A),(\rho_A,T_B))$ is performed in the neighborhood of an initial guess, giving a local linear fit (in ρ and T) to the EOS. This permits a simple root solution on the matching relations for P, u_p, and the Hugoniot relation, generating a new guess. This method generally converged within two iterations, requiring about four to six simulations for each data point.

A. Reshock with a sapphire anvil

For a set of eight points along the principal Hugoniot chosen for direct comparison with Fig. 4 of Ref. 4, we start by obtaining the reshock solutions. Since the D_2 and sapphire are in contact, the pressure and particle speed must be continuous at the interface. The reshocked deuterium pressure P_2 and particle speed u_{p2} consistent with Eq. (2) are matched to that of sapphire shocked from its initial state of $\rho_0 = 3.987$ g/cm^3. The sapphire shock response is given by $P=\rho_0 U_s u_p$, where we use a sapphire (U_s,u_p) relation $U_s = 1.247u_p + 8.081$ km/s extracted from SESAME EOS 7411

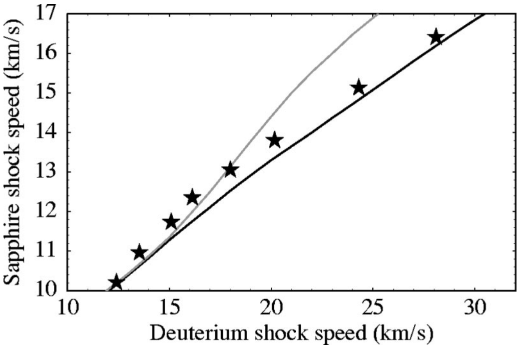

FIG. 6. Calculated shock speeds in the sapphire (stars) plotted versus the initial shock speed in the D_2. Also shown are model calculations from Kerley98 [black line (Ref. 26)] and linear mixing [gray line (Ref. 28)].

for sapphire.[41] For D_2 reshock experiments it is customary to plot the shock speed in the anvil versus the shock speed in the D_2. We show the results of these calculations (stars) in Fig. 6. The point corresponding to the lowest shock speed shown (at 12.41 km/s) is in the range of the gas-gun data and corresponds to our point at a compression of 3.236 in Fig. 3. For lower shock speeds the response is closer to that of the linear-mixing model (gray line), but for higher primary shock speeds the response shifts over toward the stiffer Kerley98 model (black line). This shift in character at the lower shock velocities appears to be emerging in previous DFT/GGA calculations of deuterium reshock (aluminum anvil) that were limited to primary shock velocities above 20 km/s.[38] PIMC results in the same paper remain nearer the SESAME curve.[27] Preliminary sapphire reshock results from Sandia's magnetically launched flyer experiments are in very good agreement with the results shown here.[42] That the re-

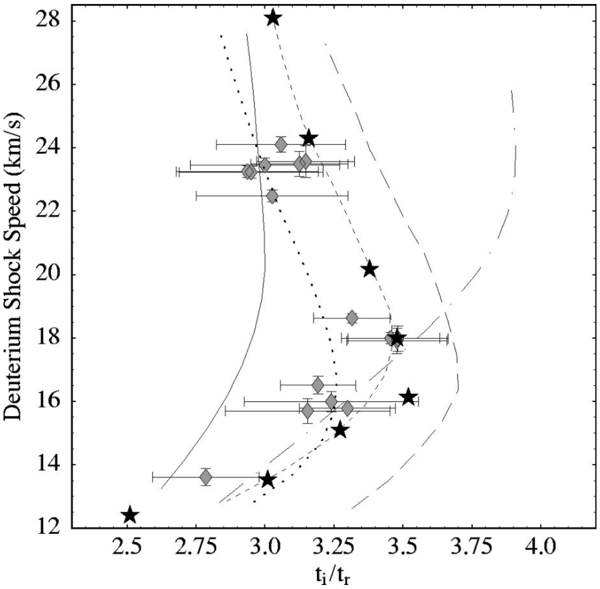

FIG. 7. Calculated reverberation timing ratios (stars) compared with magnetically launched flyer data and results of other simulations and models as a function of the initial D_2 shock speed. Symbols and lines as in Fig. 3.

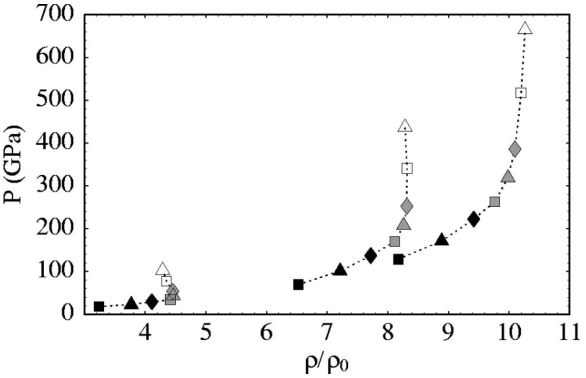

FIG. 8. Pressure versus compression ratio for the first, second, and third shocks. The symbols on the first curve (lowest compression) correspond to the primary shock states listed in Table I in the order of increasing pressure. The symbol sequence is repeated for the second- and third-shock states to identify those corresponding to the same primary shock.

sults shown here for the shock speed in sapphire are faster than those obtained with the linear-mixing model for lower shock speeds is attributable to the combination of a primary shock response very similar to linear mixing in this range, followed by a somewhat stiffer reshock than linear mixing in our calculations.

B. Reverberation timing ratios

Having obtained the reshock states (E_2,V_2,P_2), we proceed to calculate the third shock states. For this third shock, the pressure P_3 and particle speed u_{p3} consistent with Eq. (3) are matched to the aluminum response. Here we have the added complication that the aluminum response is not that of solid aluminum at ambient. Rather, it is the shock response of aluminum from the release state of the initial shock. This requires a separate aluminum response curve for each initial shock speed. For this aspect of the calculation we use the SESAME 3700 EOS for aluminum[43] to generate a set of $P(u_p;U_{s1})$ response curves for the aluminum reshocked from its primary shock release state. These response curves along with iterated solutions to Eq. (3) allow us to determine the third-shock states. (Since the aluminum and sapphire are much stiffer than the shocked deuterium, the reverberation results are rather insensitive to differences amongst the respective equations of state used for these materials.)

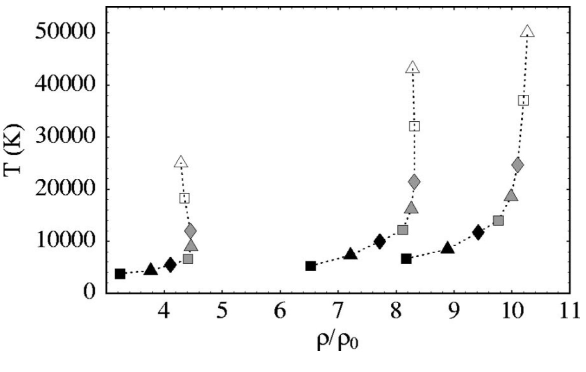

FIG. 9. Temperature versus compression ratio for the first, second, and third shocks. Symbols arranged as in Fig. 8.

TABLE I. Simulation results used to construct Figs. 6–9. The table is organized into eight groups of three, corresponding to the three successive shocks for each of the eight reverberation calculations.

U_s (km/s)	ρ/ρ_0	P (GPa)	T (K)
U_{s1}: 12.41	ρ_1/ρ_0: 3.236	P_1: 18.13	T_1: 3800
U_{s2}: 13.62	ρ_2/ρ_0: 6.526	P_2: 69.67	T_2: 5286
U_{s3}: 16.28	ρ_3/ρ_0: 8.175	P_3: 129.1	T_3: 6670
13.53	3.768	22.92	4400
15.97	7.214	101.1	7340
17.43	8.889	171.4	8495
15.10	4.108	29.37	5500
18.15	7.719	137.2	9974
18.97	9.418	222.5	11720
16.13	4.410	34.28	6600
19.90	8.116	170.1	12200
19.96	9.765	263.1	14010
18.00	4.462	42.87	8957
21.72	8.262	207.8	16208
21.42	9.983	319.1	18574
20.17	4.453	53.79	12000
23.76	8.314	252.6	21442
23.09	10.10	386.0	24675
24.30	4.349	77.40	18300
27.33	8.318	341.4	32135
25.96	10.20	517.5	37094
28.09	4.287	103.1	25000
30.80	8.285	437.3	43188
28.91	10.27	664.7	50105

Following Ref. 4, we calculate the ratio of the initial shock transit time t_i to the reverberation time t_r,

$$\frac{t_i}{t_r}\equiv\frac{t_1-t_0}{t_2-t_1}=\left[\rho_0 U_{s1}\left(\frac{1}{\rho_1 U_{s2}}+\frac{1}{\rho_2 U_{s3}}\right)\right]^{-1}, \tag{4}$$

where the t_j are the times, the ρ_j are the densities, and the U_{sj} are the relative (Lagrangian) shock speeds as shown in Fig. 5. Examination of Eq. (4) with respect to several different equations of state indicates that $U_{s3}\approx U_{s2}\approx 1.1U_{s1}$, and $\rho_2\approx 1.9\rho_1$ with only minor variations.[4] The reverberation timing ratio is therefore most sensitive to the density compression in the first shock, $t_i/t_r\sim\rho_1/\rho_0$. Since $U_{s1}=\sqrt{P_1/\rho_0}/\sqrt{1-\rho_0/\rho_1}$, the reverberation timing plot is qualitatively similar to a traditional $P(\rho)$ Hugoniot plot.

The results of the reverberation timing ratio calculations are shown in Fig. 7 plotted against the primary deuterium shock speed, with reproduced curves and data from Fig. 4 of Ref. 4. The symbols and lines are the same as in Fig. 3, however in this plot the full magnetically launched flyer dataset is shown, not the uncertainty-weighted averages. The agreement between these results and the data from the flyer experiments is very good. The greatest disagreement appears to be around the dissociation regime where our thermodynamically consistent fit (interpolated from select points for Fig. 7 and used here only for the first shock) differs from the DFT/QMD result. This is evident in Fig. 7 around a shock speed of 16 km/s. These new DFT/GGA results are in somewhat better agreement overall with the reverberation data than the tight-binding results, which one would expect to deal less accurately with the highly compressed and ionized deuterium in the second- and third-shock states.

V. TEMPERATURE AND PRESSURE STATES

The pressure and temperature states achieved in the first, second, and third shocks for the points shown in Figs. 6 and 7 are shown in Figs. 8 and 9 with connecting lines drawn to distinguish the three different shocks. (See Table I for the precise numbers, along with the second and third Lagrangian shock speeds.) From left to right in each figure the groups correspond to the first (principal Hugoniot), second (reshock), and third shocks in that order. The same symbol sequence is used in each case to indicate which points correspond to the same primary shock. Thus, the lowest point in each set (solid squares) corresponds to the first, second, and third shocks for the lowest primary shock speed in Fig. 6 (12.41 km/s), the solid triangles correspond to the next highest initial shock speed (13.53 km/s), and so forth. Those points that are represented with the same symbol as those on the primary Hugoniot are, by definition, secondary and tertiary Hugoniot points consistent with the reference state and the primary Hugoniot state.

In all cases, we find some temperature increase with each shock. However, at the lowest point shown, which is at the upper range of the gas-gun data, the temperature increase is rather modest. The primary shock achieves a temperature of 3800 K in excellent agreement with gas-gun data,[32] the reshock achieves a temperature of 5286 K, which is only 10% higher than that predicted by the linear-mixing model for the same primary shock.[32] Recall that the linear-mixing model was tuned to match reshock temperatures from gas-gun experiments.[28,32]

VI. CONCLUSIONS

Density-functional calculations of the principal Hugoniot, reshock with a sapphire anvil, and reverberation timing ratios are in very good agreement with gas-gun data and magnetically launched flyer data for density, pressure, and where available, temperature. The remaining differences in compression between these calculations and the flyer data are of the order of (3–5)%, which is in the range of a small systematic error in either U_s or u_p and not unexpected with the impedance-matching technique. The differences between calculations of the reverberation timing ratios and the corresponding data are largely consistent with the principal Hugoniot differences. Since the underlying sources of error are different, it suggests that the differences are real. The region of greatest difference is in the dissociation phase, where the electronic gap between conduction and valence bands is still open, but the thermal occupation of conduction bands is becoming significant. This is a situation where improvements to the exchange and correlation functionals (exact exchange, for example) are likely to have a significant effect on the total pressure and energy relative to the initial state. However, including exact exchange in molecular-dynamics calculations of this size is a formidable undertaking.

ACKNOWLEDGMENTS

The author would like to thank M. D. Knudson, J. R. Asay, T. A. Mehlhorn, L. A. Collins, and J. D. Kress for numerous stimulating discussions. The computations discussed here were performed on Sandia's C-Plant and QT Compaq-Alpha computer clusters. Sandia is a multiprogram laboratory operated by Sandia Corporation, a Lockheed Martin Company, for the United States Department of Energy under Contract No. DE-AC04-94AL85000.

---

*Electronic address: mpdesja@sandia.gov

[1] L.B. Da Silva, P. Celliers, G.W. Collins, K.S. Budil, N.C. Holmes, T.W. Barbee, B.A. Hammel, J.D. Kilkenny, R.J. Wallace, M. Ross, R. Cauble, A. Ng, and G. Chiu, Phys. Rev. Lett. **78**, 483 (1997).

[2] G.W. Collins, L.B. DaSilva, P. Celliers, D.M. Gold, M.E. Foord, R.J. Wallace, A. Ng, S.V. Weber, K.S. Budil, and R. Cauble, Science **281**, 1178 (1998).

[3] M.D. Knudson, D.L. Hanson, J.E. Bailey, C.A. Hall, J.R. Asay, and W.W. Anderson, Phys. Rev. Lett. **87**, 225501 (2001).

[4] M.D. Knudson, D.L. Hanson, J.E. Bailey, C.A. Hall, and J.R. Asay, Phys. Rev. Lett. **90**, 035505 (2003).

[5] W.J. Nellis, A.C. Mitchell, M. van Theil, G.J. Devine, R.J. Trainor, and N. Brown, J. Chem. Phys. **79**, 1480 (1983).

[6] N.D. Mermin, Phys. Rev. **137**, A1441 (1965).

[7] T.J. Lenosky, S.R. Bickham, J.D. Kress, and L.A. Collins, Phys. Rev. B **61**, 1 (2000).

[8] G. Galli, R.Q. Hood, A.U. Hazi, and F. Gygi, Phys. Rev. B **61**, 909 (2000).

[9] S. Bagnier, P. Blottiau, and J. Clérouin, Phys. Rev. E **63**, 015301(R) (2001).

[10] G. Kresse and J. Hafner, Phys. Rev. B **47**, 558 (1993).

[11] G. Kresse and J. Hafner, Phys. Rev. B **49**, 14 251 (1994).

[12] G. Kresse and J. Furthmüller, Comput. Mater. Sci. **6**, 15 (1996).

[13] G. Kresse and J. Furthmüller, Phys. Rev. B **54**, 11 169 (1996).

[14] Y. Wang and J.P. Perdew, Phys. Rev. B **44**, 13 298 (1991).

[15] S. Nosé, Mol. Phys. **52**, 256 (1984).

[16] S. Nosé, J. Chem. Phys. **81**, 511 (1984).

[17] W.G. Hoover, Phys. Rev. A **31**, 1695 (1985).

[18] M.C. Payne, M.P. Teter, D.C. Allen, T.A. Arias, and J.D. Joannopoulos, Rev. Mod. Phys. **64**, 1045 (1992).

[19] G. Kresse and D. Joubert, Phys. Rev. B **59**, 1758 (1999).

[20] G. Kresse and J. Hafner, J. Phys.: Condens. Matter **6**, 8245 (1994).

[21] A.M. Rappe, K.M. Rabe, E. Kaxiras, and J.D. Joannopoulos, Phys. Rev. B **41**, 1227 (1990).

[22] A. Baldereschi, Phys. Rev. B **7**, 5215 (1973).

[23] H.J. Monkhorst and J.D. Pack, Phys. Rev. B **13**, 5188 (1976).

[24] Y. B. Zeldovich and Y. P. Raizer, *Physics of Shock Waves and High-Temperature Hydrodynamic Phenomena* (Academic Press, New York, 1966).

[25] W. Kolos and L. Wolniewicz, J. Chem. Phys. **41**, 3674 (1964).

[26] G. I. Kerley (private communication).

[27] G. I. Kerley, in *Molecular Based Study of Fluids*, edited by J. M. Hail and G. A. Mansoori (ACS, Washington, DC, 1983), p. 107.

[28] M. Ross, Phys. Rev. B **58**, 669 (1998).

[29] T.J. Lenosky, J.D. Kress, and L.A. Collins, Phys. Rev. B **56**, 5164 (1997).

[30] B. Militzer and D.M. Ceperley, Phys. Rev. Lett. **85**, 1890 (2000).

[31] J. C. Slater, *Quantum Theory of Matter* (McGraw-Hill, New York, 1968).

[32] N.C. Holmes, M. Ross, and W.J. Nellis, Phys. Rev. B **52**, 15 835 (1995).

[33] F. Gygi and G. Galli, Phys. Rev. B **65**, 220102(R) (2002).

[34] R. Car and M. Parrinello, Phys. Rev. Lett. **55**, 2471 (1985).

[35] H. Juranek, R. Redmer, and Y. Rosenfeld, J. Chem. Phys. **117**, 1768 (2002).

[36] T.J. Lenosky, J.D. Kress, L.A. Collins, and I. Kwon, Phys. Rev. B **55**, R11 907 (1997).

[37] L.A. Collins, S.R. Bickham, J.D. Kress, S. Mazevet, T.J. Lenosky, N.J. Troullier, and W. Windl, Phys. Rev. B **63**, 184110 (2001).

[38] B. Militzer, D.M. Ceperley, J.D. Kress, J.D. Johnson, L.A. Collins, and S. Mazevet, Phys. Rev. Lett. **87**, 275502 (2001).

[39] D. Saumon and G. Chabrier, Phys. Rev. A **46**, 2084 (1992).

[40] W.J. Nellis, Phys. Rev. Lett. **89**, 165502 (2002).

[41] *SESAME: The Los Alamos National Laboratory Equation of State Database*, LANL Report No. LA-UR-92-3407, 1992 (unpublished).

[42] M. Knudson (private communication).

[43] G. I. Kerley, Kerley Publishing Services Report No. KPS98-1, 1998 (unpublished).